

Controlled growth of PbI₂ nanoplates for rapid preparation of CH₃NH₃PbI₃ in planar perovskite solar cells

Fan Fu^{1,*}, Lukas Kranz¹, Songhak Yoon², Johannes Loeckinger¹, Timo Jäger¹, Julian Perrenoud¹, Thomas Feuer¹, Christina Gretener¹, Stephan Buecheler^{1,*}, and Ayodhya N. Tiwari¹

¹ Laboratory for Thin Films and Photovoltaics, Empa – Swiss Federal Laboratories for Materials Science and Technology, Ueberlandstrasse 129, 8600 Dübendorf, Switzerland

² Laboratory of Materials for Energy Conversion, Empa – Swiss Federal Laboratories for Materials Science and Technology, Ueberlandstrasse 129, 8600 Dübendorf, Switzerland

Corresponding authors: Fan Fu, e-mail: fan.fu@empa.ch, phone: +41 58 765 61 84

Stephan Buecheler, email: Stephan.buecheler@empa.ch, phone: +41 58 765 6107

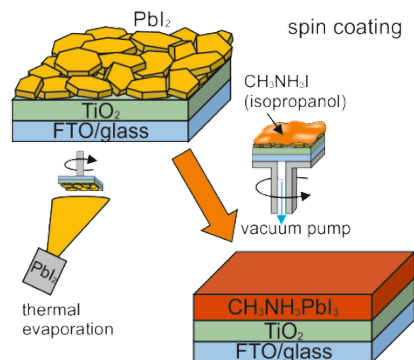
Received ZZZ, revised ZZZ, accepted ZZZ

Published online ZZZ (Dates will be provided by the publisher.)

Keywords PbI₂ nanoplates, CH₃NH₃PbI₃, perovskite solar cells, rapid preparation.

Absorbers for planar perovskite solar cells are often prepared by two-step deposition methods, where a thick compact PbI₂ layer is deposited followed by conversion to perovskite using CH₃NH₃I solution. The surface of the precursor layer quickly reacts with the CH₃NH₃I solution, which hinders further diffusion of CH₃NH₃I into the layer, consequently leading to significant amounts of residual PbI₂ at room temperature. Here, we report a novel concept that employs a porous nanostructured PbI₂ layer consisting of nanoplates to rapidly prepare single phase perovskite layer. The non-compact nanoplate morphology is achieved in a controllable manner by thermal evaporation of PbI₂ on TiO₂ coated FTO substrate and allows easy penetration of CH₃NH₃I solution into the whole PbI₂ layer, thus facilitating fast and complete conversion. The amount of PbI₂ residual can be controlled by varying the CH₃NH₃I concentration. The growth of the nanoplates is governed by the intrinsic crystallographic structure of the deposited material, crystal characteristics of the underlying substrate, and deposition method. The introduced process enables planar perovskite solar cells with efficiency of 8.6 % measured at

maximum power point. This work opens a new route for rapid preparation of other 3-dimensional organic-inorganic hybrid perovskites by rational tailoring the metal halide morphology.



Copyright line will be provided by the publisher

1 Introduction Methylammonium lead trihalide (general formula CH₃NH₃PbX₃, X = Cl, Br or I) perovskite solar cells have emerged as a highly competitive photovoltaic technology.^[1] Owing to their distinguished properties, such as strong optical absorption,^[1] high carrier mobility,^[2] and long carrier diffusion length,^[3] perovskite solar cells have experienced unprecedented advancements since

Kojima *et al.*'s pioneering work with power conversion efficiency soaring from 3.8% to the current record efficiency of 20.1% within the past 5 years.^[4-9] While perovskite solar cells were first introduced with a mesoporous scaffold, and this type of architecture continues to offer high efficiency,^[10] efficient planar devices have also drawn considerable attention due to the simple device architecture.^[11-14] For

Copyright line will be provided by the publisher

planar perovskite solar cells, a flat and homogeneous perovskite layer is critical for achieving high efficiency. Liu *et al.* have demonstrated that a homogeneous perovskite film with full coverage of the substrate can be obtained by dual-source thermal evaporation resulting in a high power conversion efficiency of 15.4%.^[6] Although this is a promising approach, the control of $\text{CH}_3\text{NH}_3\text{I}$ evaporation can be problematic due to the high vapor pressure and easy decomposition of the organic salt.^[15] Perovskite films deposited from simple one-step spin coating often suffered from uncovered pin-holes and non-homogeneity due to the rapid uncontrollable precipitation from the blend precursors.^[8, 16] In this context, Burschka *et al.* used a sequential deposition where PbI_2 was first spin casted onto the substrate followed by dipping into a $\text{CH}_3\text{NH}_3\text{I}$ solution.^[7] Similarly, other two-step deposition methods like vapor-assisted solution process or sequential spin coating were also used to produce perovskite films and deliver impressively high efficiencies up to 17%.^[17-20]

However, complete conversion to perovskite from a thick planar PbI_2 (200~300 nm) layer is not easy at room temperature. Previous studies have shown that complete conversion of a planar PbI_2 film to perovskite by dipping into $\text{CH}_3\text{NH}_3\text{I}$ solution usually takes long time at room temperature or several minutes (~5 min) at elevated temperatures (~60 °C).^[7, 21-22] In sequential spin coating, a post-deposition annealing step at 100 °C is required to fully convert PbI_2 into perovskite.^[18] It is widely accepted that a thin layer of $\text{CH}_3\text{NH}_3\text{PbI}_3$ immediately forms upon addition of $\text{CH}_3\text{NH}_3\text{I}$ containing solution to a PbI_2 layer, which renders further diffusion of $\text{CH}_3\text{NH}_3\text{I}$ into PbI_2 more difficult due to the lack of van der Waals gaps in three-dimensional $\text{CH}_3\text{NH}_3\text{PbI}_3$.^[7, 15, 18] Due to the slow diffusion of $\text{CH}_3\text{NH}_3\text{I}$ upon surface reaction, previously reported sequential deposition methods necessitate long reaction time or intentional heating to form a single phase planar perovskite layer. This often results in dissolving and/or peeling-off of the perovskite layer into solution, thus leading to a rough surface and poor device performance.^[18, 21, 23] Besides, the deposition of fully covering PbI_2 layers over large area by spin coating is still quite a challenge mainly owing to the low solubility in the commonly used solvent *N,N*-dimethylformamide (DMF).^[24]

Here we report a novel concept that employs a porous PbI_2 layer consisting of nanoplates to rapidly prepare a single phase perovskite layer for planar perovskite solar cells. The non-compact nanoplate morphology of the PbI_2 layer is achieved in a controllable manner by thermal evaporation onto TiO_2 coated FTO/glass substrate and this unique microstructure allows easy penetration of $\text{CH}_3\text{NH}_3\text{I}$ solution into the whole PbI_2 layer, thus facilitating fast and complete conversion at room temperature. We unravel that the intrinsic crystallographic structure of the deposited material, crystal characteristics of the underlying substrate, and deposition method are three key parameters

that govern the growth of nanoplates and elucidate the formation mechanism of nanoplates. The perovskite film prepared in this work enabled us to fabricate planar perovskite solar cells with steady-state output efficiency of 8.6% under AM1.5G simulated one sun illumination.

2 Experimentals

2.1 Perovskite solar cell fabrication Perovskite solar cells were grown on FTO coated glass (Pilkington, 15 Ohm sq^{-1}) substrates. Substrates were washed by hand followed by ultrasonic soap and water baths. Subsequently, the FTO glasses were subjected to O_2 plasma treatment for 10 min, after which a 70 nm thick (determined from SEM image) compact TiO_2 layer was deposited by reactive DC sputtering followed by annealing at 500 °C for 45 min in N_2 atmosphere. A PbI_2 film was thermally evaporated on rotating TiO_2 /FTO/glass substrates at a deposition pressure of $2 - 5 \times 10^{-8}$ mbar. Unless otherwise noted, the deposition rate is controlled within $1.2 - 1.6 \text{ \AA s}^{-1}$, which was monitored by a quartz crystal microbalance. After the PbI_2 deposition, the samples were subsequently transferred into a N_2 filled glove-box for further processing. The perovskite layer was formed by spin coating of $\text{CH}_3\text{NH}_3\text{I}$ (Dyesol, 99.9%) in 2-propanol. The solution was first spread to cover the whole substrate, followed by immediately starting the rotation (500 rpm for 3 s, then 4000 rpm for 40 s). The as-prepared films were annealed at 100 °C for 30 min on a hotplate. After annealing, the samples were cooled down to room temperature and 30 μL of a Spiro-OMeTAD solution (78.8 mg (2, 2', 7, 7'-tetrakis-(*N,N*-di-*p*-methoxyphenylamine)-9, 9'-spirobifluorene) (Spiro-OMeTAD) (Merck), 17.5 μL lithium-bis(trifluoromethanesulfonyl)imide (Li-TFSI, Sigma-Aldrich) solution (520 mg Li-TFSI in 1 mL acetonitrile, Sigma-Aldrich), and 28.5 μL 4-tertbutylpyridine (TBP, Sigma-Aldrich) all dissolved in 1040 μL chlorobenzene (Sigma-Aldrich) was spin coated at 2000 rpm for 20s. After Spiro-OMeTAD deposition, the samples were stored in a drybox for ~2 h. The devices were finished by evaporating 60 nm Au through a metal mask under high vacuum, defining the cell area at 0.15 cm^2 .

ZnO is deposited by radio-frequency (RF) sputtering. The PCBM layer is prepared by spin coating of 30 μL of PCBM solution (20 mg/mL in chlorobenzene) on FTO/glass substrate at 2000 rpm for 40 s. The PEDOT:PSS is prepared by spin coating on ITO/glass substrate at 5000 rpm for 40 s. CuSCN is deposited by spin coating of 100 μL saturated solution in *n*-propyl sulphide on FTO/glass substrate at 2000 rpm for 40 s. Zn(O,S) was grown by chemical bath deposition (CBD) in 25 minutes from a solution of thiourea (0.6 M), ZnSO_4 (0.15 M) and ammonium hydroxide (4 M) at 80 °C. For CdS a mixture of cadmium acetate (1.8 mM), thiourea (22 mM) and am-

monium hydroxide (2 M $[\text{NH}_3]$) was allowed to react for 11 minutes at 70 °C.

2.2 Characterization X-ray diffraction patterns were obtained in Bragg-Brentano geometry by using a X'Pert PRO θ -2 θ scan ($\text{Cu-K}\alpha_1$ radiation, $\lambda = 1.5406 \text{ \AA}$) from 10 to 60° (2 θ) with a step interval of 0.0167°. Le Bail fitting was used to determine the lattice parameters. The microstructure of the samples were investigated with a Nova NanoSem230 FEI using 5 kV voltage. A thin layer of C or Pt was deposited on top of the sample to avoid charging effect. The transmittance (T) and reflectance (R) spectra were acquired using a UV-Vis-NIR spectrophotometer (Shimadzu UV-3600) equipped with an integrating sphere. Absorption A is calculated using the following formula: $A = 1 - T - R$.

2.3 Solar cells performance The current density-voltage characteristics of perovskite solar cells were measured under standard AM1.5G one sun illumination with 1000 W m^{-2} intensity using a Keithley 2400 source. The J - V measurements are performed in both forward (1.2 V to -0.1 V) and backward (-0.1 V to 1.2 V) direction at a scan rate and delay time of 0.3 Vs^{-1} and 10 ms. The illumination intensity was calibrated using a Si solar cell. The steady-state efficiency is evaluated by using a maximum power point tracker algorithm with constant AM1.5G illumination.

3 Results and discussion

3.1 Microstructure and composition of $\text{CH}_3\text{NH}_3\text{PbI}_3$ Figure 1 shows a schematic illustration of the novel perovskite preparation process. The perovskite deposition is performed on a TiO_2/FTO (fluorine-doped tin oxide) coated glass substrate. A PbI_2 layer with a nominal thickness of 200 nm (controlled by quartz crystal microbalance assuming dense structure) is deposited on compact TiO_2 via thermal evaporation. Subsequently, solution of $\text{CH}_3\text{NH}_3\text{I}$ in 2-propanol is added by spin coating to form the perovskite layer. Immediately after spin coating, the as-prepared layer shows brown color at room temperature (Figure S1, supporting information), which is the typical color for the targeted perovskite material. More detailed procedures can be found in the experimental section.

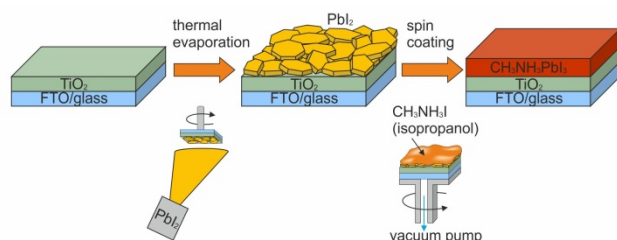


Figure 1 Schematic illustration of the rapid room temperature preparation of the perovskite film on compact TiO_2 coated FTO/glass substrate.

As mentioned above, previously reported sequential deposition methods employing planar PbI_2 layer require long reaction time at room temperature or elevated reaction temperature ($\sim 60^\circ\text{C}$) to form a single phase planar perovskite layer.^[7, 18, 21-22] We propose that fast and complete conversion to perovskite at room temperature is possible by tailoring the morphology of the PbI_2 layer. Recent studies have shown that PbI_2 thin films deposited by spin coating usually have a compact morphology regardless of the employed substrates (such as glass, PEDOT:PSS/ITO, TiO_2/FTO).^[7, 18, 22] Likewise, thermally evaporated PbI_2 film on glass substrate also displayed a similar compact morphology with small grains uniformly distributed on the surface.^[21] Here we demonstrate that porous planar PbI_2 film comprising nanoplates can be obtained in a controllable manner via thermal evaporation by choosing a suitable substrate.

The scanning electron microscopy (SEM) images in Figure 2 reveal the microstructure evolution from the evaporated PbI_2 film to corresponding perovskite layers without and with annealing step on a TiO_2/FTO /glass substrate. It is evident from Figure 2(a) that the evaporated PbI_2 layer is composed of nanoplates with an average diameter of around 250 nm and a thickness of around 25 nm, which are uniformly distributed over a large area. Many nanoplates have a well-defined hexagonal shape. The size-to-thickness aspect ratio is around 10:1, indicating a faster growth rate within the basal plane as compared to the perpendicular $[00l]$ direction. This is attributed to the minimization of the surface energy.^[25] The majority of the nanoplates are loosely aligned parallel to the substrate or tilted with only a small angle with respect to the substrate, and only a small fraction aligning perpendicular to the substrate. The unique arrangement of these nanoplates creates voids in-between, which is beneficial for fast reaction kinetics as the $\text{CH}_3\text{NH}_3\text{I}$ can easily penetrate through the voids to reach the nanoplates close to the underlying substrate, and thereby facilitating fast and complete conversion. The thickness of the PbI_2 film is around 350-400 nm (see Figure 2(a) cross sectional image), which is larger than we expected due to the porous microstructure. As the quartz crystal microbalance measures the deposited mass, the deposited 200 nm thickness only corresponds to the thickness of a compact layer.

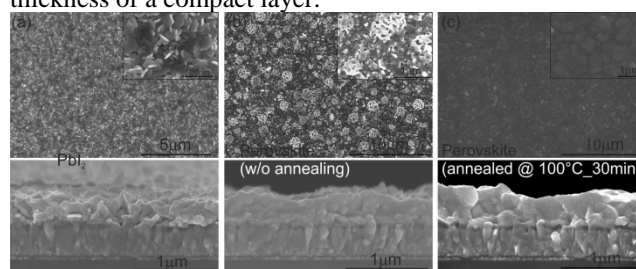


Figure 2 Top view and cross-sectional SEM images of (a) thermal evaporated PbI_2 film, (b) as-deposited perovskite film without annealing, and (c) perovskite film annealed at 100 °C for 30 min on $\text{TiO}_2/\text{FTO}/\text{glass}$.

The PbI_2 nanoplates were subjected to spin coating of the $\text{CH}_3\text{NH}_3\text{I}$ solution at room temperature, and the corresponding SEM images are displayed in Figure 2(b). The morphology of spin casted layer is quite different from the parent PbI_2 . Instead of nanoplates, there are plenty of porous open dome-shaped structures distributed uniformly on the surface, which are formed due to the evaporation of solvent during spinning. Regardless of the porous surface morphology, the cross-sectional image shows a compact layer composed of irregularly shaped grains. The thickness of the as-deposited perovskite layer is comparable to the thickness of the parent PbI_2 layer, which is noticeably different from other reported two-step methods where the perovskite thickness is usually at least 2 fold of the original PbX_2 ($X = \text{I}, \text{Cl}$) due to the compact layer employed.^[18-19, 23] This confirms the porous structure of the PbI_2 layer employed in this work, which turned into compact perovskite layer after conversion. After 30 min annealing at 100 °C, the porous dome disappeared and a compact surface formed as shown in Figure 2(c). Besides, the grain size increased dramatically compared to the as-deposited perovskite layer, which is beneficial for the photovoltaic performance as will be discussed later.

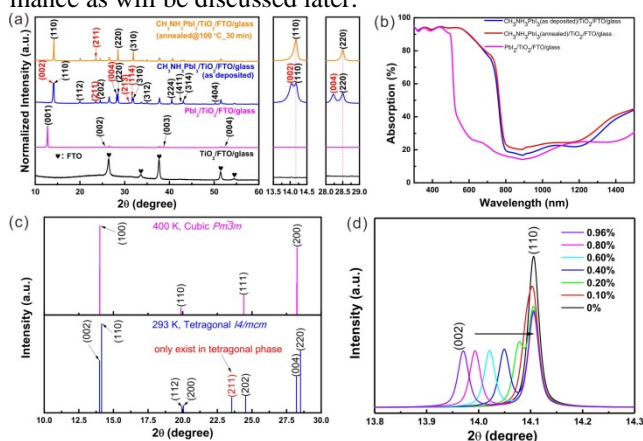


Figure 3 X-ray diffraction (XRD) patterns and absorption spectrum of PbI_2 and corresponding perovskite film. (a) XRD and (b) absorption spectrum of PbI_2 and perovskite film without and with annealing. (c) Simulated XRD patterns of tetragonal and cubic structure of $\text{CH}_3\text{NH}_3\text{PbI}_3$. (d) Degree of tetragonal distortion for as-deposited perovskite film.

To verify the proposed concept of using PbI_2 nanoplates for the rapid growth of a single-phase perovskite layer, we obtained X-ray diffraction (XRD) patterns and absorption spectra of samples after $\text{CH}_3\text{NH}_3\text{I}$ spin coating without and with annealing as depicted in Figure 3. The diffraction reflections of the as-deposited film in Figure 3(a) can be well indexed to single phase $\text{CH}_3\text{NH}_3\text{PbI}_3$

without any detectable secondary PbI_2 phase.^[21] To achieve single phase $\text{CH}_3\text{NH}_3\text{PbI}_3$, the concentration of $\text{CH}_3\text{NH}_3\text{I}$ in the spin coating solution is optimized to be 45 mg mL^{-1} (Figure S2, supporting information). The perovskite layer retains its tetragonal phase after annealing at 100 °C for 30 minutes. The absorption spectrum of the as-deposited film exhibits high absorption over the whole visible light region and a cut-off which corresponds to the perovskite band gap of 1.57 eV, as can be seen from Figure 3(b). The absorption spectrum of the same sample annealed at 100 °C for 30 min remained almost unchanged. The XRD and absorption measurements were repeated on different samples to corroborate the aforementioned findings (Figure S3, supporting information). These results clearly demonstrate that the introduced novel strategy permits the rapid formation of single phase planar perovskite films from thick PbI_2 layer at room temperature.

To understand the perovskite formation mechanism, we carefully scrutinized the phase composition of the evaporated PbI_2 and perovskite layers. The XRD pattern of the evaporated PbI_2 on a $\text{TiO}_2/\text{FTO}/\text{glass}$ substrate is shown in Figure 3(a). The diffraction patterns are dominated by (00 l) ($l = 1, 2, 3, 4$) lattice planes, indicating a strong preferential orientation along the c -axis in evaporated PbI_2 films, which is consistent with the observed PbI_2 nanoplate morphology. After $\text{CH}_3\text{NH}_3\text{I}$ spin coating, the PbI_2 film fully converted into perovskite and its phase is investigated in more detail. At room temperature, $\text{CH}_3\text{NH}_3\text{PbI}_3$ generally adopts a tetragonal crystal structure (space group: $I4/mcm$) characterized by the appearance of (211) and (213) reflections at 23.5° and 31.0° , respectively.^[26] Furthermore, at around 14.2° and 28.4° double-peaks exist in the tetragonal phase and should be distinguishable according to simulated XRD patterns in Figure 3(c). This result is also confirmed by previously reported experimental XRD patterns.^[21] The XRD patterns in our as-deposited perovskite films (Figure 3(a) and magnified plots) grown from PbI_2 nanoplates clearly show both of these features, manifesting its tetragonal structure. Magnified plots in Figure 3(a) further show a strong relative intensity enhancement of (002) and (004) reflections in the as-deposited perovskite compared to the powder XRD pattern for random orientation. This indicates a partial preservation of the c -axis orientation of the parent PbI_2 , matching well to the characteristic feature of in-situ intercalation formation mechanism.^[27] After annealing at 100 °C for 30 min the reflections at (002), (004) and (213) are not visible anymore. But the (211) reflection, which only exists in the tetragonal structure, is still preserved, thus indicating a recrystallization process but an unchanged tetragonal crystal structure. This recrystallization also implies that the crystal structure in the as-deposited perovskite film is not in equilibrium condition, but distorts to some extent. With the simulated XRD patterns, we were able to estimate the degree of tetragonal distortion in the as-deposited layers to be ~ 0.96% (see Figure 3(d)). The degree of tetragonal distortion

tion is defined here as: $\delta = (\frac{c/a}{\sqrt{2}} - 1) \times 100\delta = (\frac{c/a}{\sqrt{2}} - 1) \times d$. Detailed calculation is shown in Table 1. We found that for a very small tetragonal distortion, the (002) and (110) reflections start to merge into one peak. This also explains why only the (110) reflection is observed in numerous XRD patterns reported previously, where generally an annealing step is applied during the formation of the perovskite layer.^[17-18] But it should be noted that the crystal structure of as-synthesized perovskite film is still tetragonal at room temperature.

Table 1 The influence of a tetragonal distortion δ on the XRD patterns. In order to illustrate the influence of a tetragonal distortion on the XRD patterns, lattice parameter a was kept constant and c was gradually reduced. The lattice parameters $a = 8.8722 \text{ \AA}$ and $c = 12.6680 \text{ \AA}$ are extracted from Le bail fit of the as-deposited film, consistent with a degree of tetragonal distortion of 0.96%. Crystallographic data used for XRD pattern simulation.

Degree of tetragonal distortion δ (%) ^a	Lattice parameter c (Å)	c/a
0.96	12.6680	1.4278
0.80	12.6476	1.4255
0.60	12.6225	1.4227
0.40	12.5974	1.4199
0.20	12.5723	1.4170
0.10	12.5597	1.4156
0	12.5472	$\sqrt{2}$ ^b

Space group symmetry: $I4/mcm$

^a Degree of tetragonal distortion is defined as: $\delta = (\frac{c/a}{\sqrt{2}} - 1) \times 100$

^b $\sqrt{2}$ is assumed to be the lower boundary value for the tetragonal structure. It corresponds to a tetragonal distortion of 0%, and can be explained by a cubic structure.

3.2 Controlled growth of PbI₂ nanoplates and formation mechanism

The porous nanostructured morphology of the PbI₂ layer is critical for the successful implementation of the novel concept described above. Therefore, it is of paramount importance to identify the key parameters that dominate the growth of the porous planar PbI₂ film comprising nanoplates and to unravel the formation mechanism of nanoplates in order to gain better control over the growth of the desired morphology.

3.2.1 Effect of intrinsic crystallographic structure of the lead halide

Figure 4 shows the crystal structure and SEM images of thermally evaporated PbI₂, PbBr₂, and PbCl₂ on TiO₂/FTO/glass substrate. For comparison, the deposition conditions, such as deposition rate and substrate temperature, are kept the same for all three materials. Thermally evaporated PbI₂ layer shows the above described nanoplates on TiO₂/FTO/glass substrate, while layers obtained from both PbBr₂ and PbCl₂ form compact

layers with grain sizes of several hundred nanometers on the same substrate. Presumably, the formation of nanoplates in PbI₂ film is associated with its unique anisotropic layered structure.^[28] As shown in Figure 4(a), PbI₂ comprises of hexagonally close packed I-Pb-I monolayers stacking along c -axis which are separated by a van-der-Waals gap in between.^[28] This layered structure results in faster growth in the basal plane (lateral direction) compared to the c -axis (vertical direction), as the crystalline facets tend to develop low-index planes to minimize the surface energy.^[29] For PbBr₂ and PbCl₂, their crystal structure extend to all three spatial directions, therefore no strong preferential growth direction is favored during the layer formation. Thus, it can be concluded that the preferential growth along one specific direction is critical for the formation of nanoplates, which will be discussed in more detail in section 3.2.4.

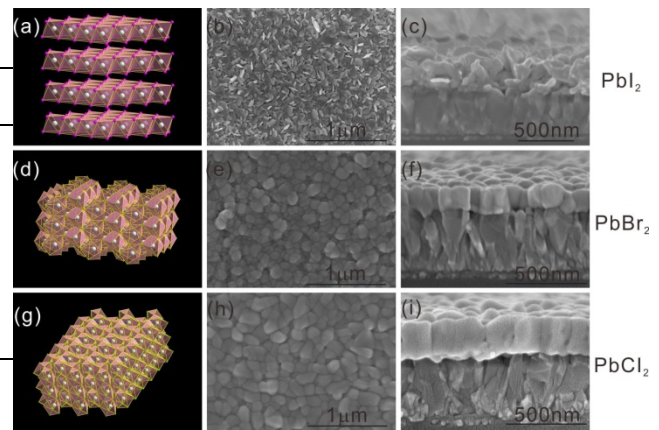


Figure 4 Crystal structure and microstructure of thermal evaporated PbX₂ (X = I, Br, Cl) on TiO₂/FTO/glass substrate. The substrate temperature is room temperature, and the deposition rate is controlled to be around 1.5 \AA s^{-1} for all the films. (a)-(c) The crystal structure and SEM images for PbI₂ film, (d)-(f) the crystal structure and SEM images for PbBr₂ film, (g)-(i) the crystal structure and SEM images for PbCl₂ film.

3.2.2 Effects of substrate crystal characteristics

Besides the intrinsic crystal structure, the substrate characteristic plays a key role in determining the PbI₂ morphology. In order to investigate the role of the substrate, PbI₂ layers were deposited on various substrate layers, including electron and hole transporting materials, under identical thermal evaporation conditions. The surface properties of the selected underlying substrate materials vary substantially from each other, but they can be roughly classified into crystalline substrates and amorphous ones.

From Figure 5 we can conclude that polycrystalline substrates, such as TiO₂, ZnO, CdS, Zn(O,S), and FTO facilitate the growth of porous plate-like microstructures; while amorphous substrates, like CuSCN, PEDOT:PSS,

PCBM and glass, lead to the growth of compact PbI₂ layers

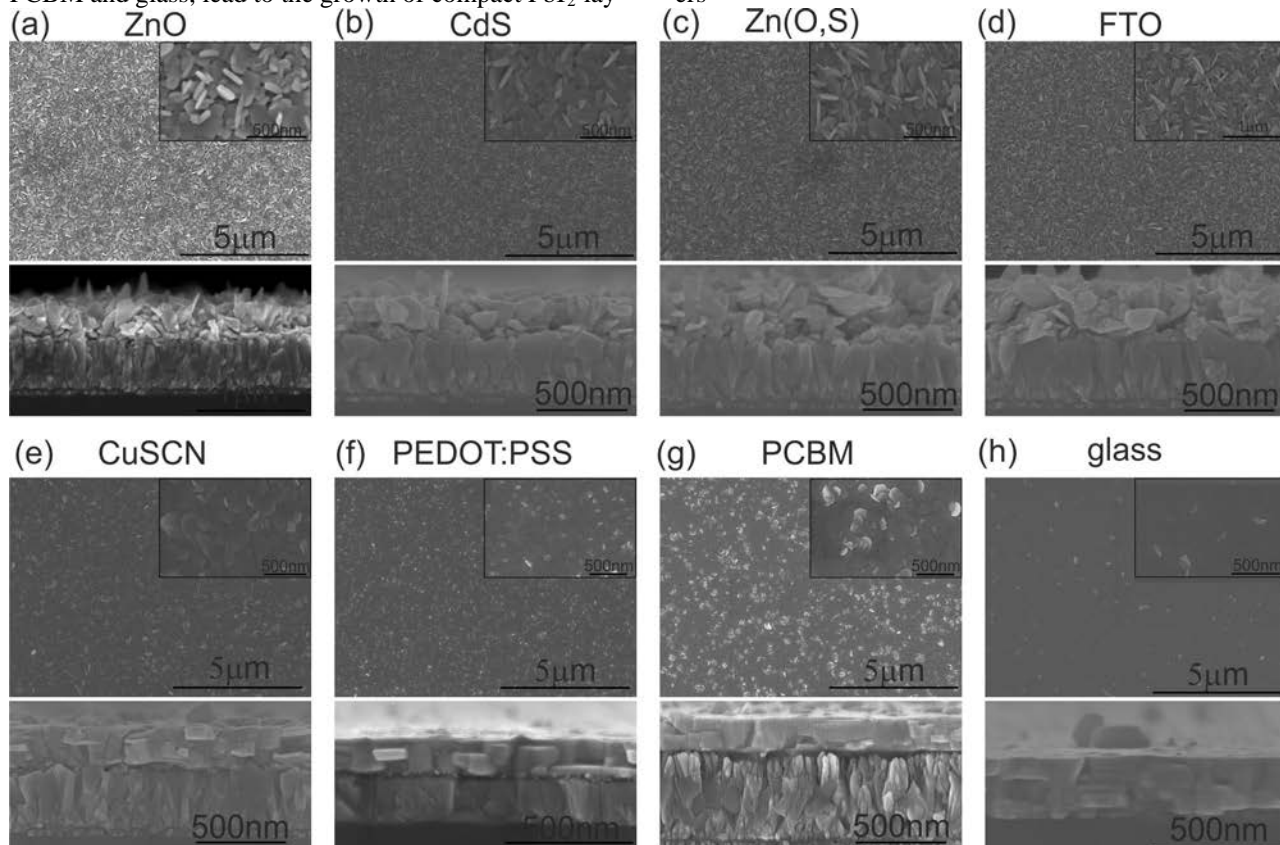


Figure 5 The top view and cross-sectional SEM images of PbI₂ films on various substrates. The under layer below PbI₂ is (a) ZnO/FTO, (b) CdS/FTO, (c) Zn(O,S)/FTO, (d) FTO, (e) CuSCN/FTO, (f) PEDOT:PSS/ITO, (g) PCBM/ZnO/FTO, and (h) glass. The CdS and Zn(O,S) are prepared by chemical bath deposition. The CuSCN, PEDOT:PSS, and PCBM are prepared by spin coating.

Such compact layers resulted in significant amounts of residual PbI₂ after CH₃NH₃I spin coating as shown in Figure S4 in supporting information, which agrees well with the previous finding that the penetration depth of CH₃NH₃I into compact planar PbI₂ layer is limited to a few tens of nanometer from the surface.^[7, 18, 21] These results unarguably show that it is essential to select an appropriate underlying substrate with tailored surface properties in order to allow the growth of the desired loosely stacked PbI₂ nanoplates.

3.2.3 Effect of deposition method and condition

Next to the crystal characteristic of substrates, the preparation method and conditions can also strongly influence nanoplates' formation. Figure 6 shows the effects of preparation methods and deposition conditions on the microstructure of PbI₂ on TiO₂/FTO/glass substrate. The morphology of spin coated PbI₂ in Figure 6(a) displays a flat film with plenty of voids on the surface, which is similar to reported morphology.^[18] The inset and cross-sectional images indicate that the individual voids do not penetrate through the entire layer thickness. Figure 6(b)-(d) present the SEM images for thermal evaporated PbI₂ film under different deposition rates and substrate temperatures.

The deposition rate can be easily tuned with high precision by controlling the source temperature. By varying the deposition rate and substrate temperature, the size, shape, and arrangement of the nano-plates can be controlled. When the rate is lowered down to 0.85 Å s⁻¹, the size of the nanoplate is similar compared with that of the normal deposition rate 1.4 Å s⁻¹, but the fraction of vertically aligned nanoplates decreased drastically as shown in the inset of Figure 6(b). When the rate is increased up to 6 Å s⁻¹, the size of nanoplates increased to several microns as seen from both top-view and cross-sectional images in Figure 6(c). Meanwhile, the percentage of vertically aligned nanoplates also increased substantially. This value can be regarded as an indicator of porosity of the planar layer. Thus, nanoplate size and porosity of the film could be controlled by manipulating the evaporation rate. When heating the substrate temperature to 100 °C during deposition, the size of nanoplate remained the same, but parts of the nanoplates exhibit distorted shape instead of flat plate shape, as can be seen in inset of Figure 6(d). Therefore, the choice of deposition technique, e.g., spin coating or thermal evaporation, is a

critical factor for the nanoplate formation. In addition, depending on the deposition conditions, such as evaporation rate and substrate temperature, the size and shape of the nanoplates, and porosity of the nanostructured layer could be controlled.

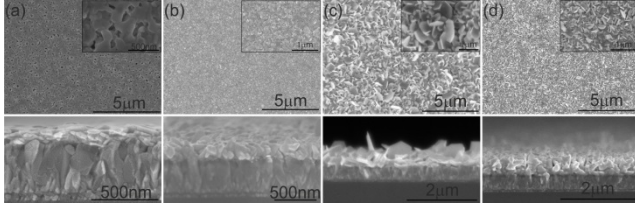


Figure 5. Influence of preparation conditions on PbI_2 microstructure on $\text{TiO}_2/\text{FTO}/\text{glass}$ substrate. (a) Spin coated PbI_2 , 100 μL of PbI_2 solution (1mM in DMF) was spin coated at 3000 rpm for 40 s. (b) Thermal evaporated PbI_2 , the deposition rate is 0.85 Å s^{-1} and substrate temperature is room temperature. (c) Thermal evaporated PbI_2 , the deposition rate is 6 Å s^{-1} and substrate temperature is room temperature. (d) Thermal evaporated PbI_2 , the deposition rate is 1.4 Å s^{-1} and substrate temperature is 100°C .

3.2.4 PbI_2 nanoplates formation mechanism

From the above observations and discussions we can conclude that the formation of PbI_2 nanoplates is primarily determined together by the crystallographic structure of the deposited material itself, crystal characteristics of the underlying substrates, and preparation techniques. In light of these experimental results, schematic illustration in Figure 7 is proposed to elucidate the PbI_2 nanoplates' formation mechanism. In the case of polycrystalline PbI_2 film prepared by thermal evaporation, the PbI_2 partially wet the substrate surface on which it deposited. In this case, the equilibrium contact angle θ is determined together by the free surface energy of the particle γ_f , the interface free energy γ_i , and the substrate surface free energy γ_s as illustrated in Figure 7(a).^[30] The interface free energy is not only dependent on the crystallographic orientation of the particle, but also partly influenced by the crystal structure of the substrate.^[31] In the course of coalescence of islands, the surface and interface energy anisotropy provides the primarily driving force, thus the grains with minimum value of combined surface and interface energy are energetically favored and thus can grow preferentially.^[31] Let us consider a coordinate system for the deposited PbI_2 particle with one axis normal to the substrate as shown in Figure 7(a). On the one hand, when the substrate is amorphous, the substrate surface energy γ_s is isotropic and the interface energy γ_i depends on the lattice rotations through β and δ , but not α as shown in Figure 7(b).^[32] As the PbI_2 forms a layered structure as shown in Figure 4(a), there is a preferential growth along the basal plane. In this scenario, the minimization of combined surface and interface energy will result in preferential growth parallel to the surface of

substrate.^[32] This can explain the compact layer structure observed in PbI_2 grown on amorphous substrates. On the other hand, when the substrate is crystalline, the substrate surface energy γ_s and interface energy γ_i are both anisotropic, then the rotation along α will also contribute to the γ_i as shown in Figure 7(c).^[32] In this case, minimization of combined surface and interface energy will lead to certain in-plane orientation,^[32] which allows certain amount of nanoplates grow tilted or vertically aligned. When the tilted or vertically nanoplates cross each other during the growth, lots of void would be created in-between. This accounts for the observation of lots of porous PbI_2 layer with tilt or even vertically aligned nanoplates on crystalline substrates. This also agrees well with the observed porous and compact PbI_2 layers in this work.

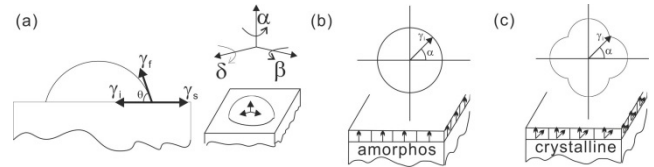


Figure 7 The schematic illustration of nanoplate formation mechanism and XRD patterns of PbI_2 on different substrates. (a) A semi-spherical cap shape particle partially wets the substrate surface. θ is the equilibrium contact angle, γ_f , γ_i , γ_s are the particle free surface energy, interface free energy and the substrate surface free energy, respectively. (b) The illustration of polycrystalline film grown on amorphous substrate. (c) The illustration of polycrystalline film grown on crystalline substrate.

3.3 Photovoltaic performance of planar perovskite solar cell

The perovskite grown by the herein described preparation method was used to fabricate solar cells. The planar perovskite device has a cell structure of $\text{glass}/\text{FTO}/\text{TiO}_2/\text{CH}_3\text{NH}_3\text{PbI}_3/\text{Spiro-OMeTAD}/\text{Au}$ as shown in Figure 8(a). The photovoltaic performances of devices without and with perovskite annealing step are shown in Figure 8(b). Both cells exhibited strong hysteresis in current density-voltage (J - V) curve, i.e. the J - V curve is influenced by measurement parameters like sweep direction and scan rate.^[33] The device without perovskite annealing step shows J_{sc} of 8.8 mA/cm^2 , V_{oc} of 0.957 V , and FF of 55.2% , from backward measurement (forward bias to short circuit). For the cells with perovskite annealing step exhibits a J_{sc} of 20.7 mA/cm^2 , V_{oc} of 1.053 V , and FF of 65.2% , from backward measured J - V curve. In general, the devices with perovskite annealing exhibit higher V_{oc} , J_{sc} , and FF compared with devices without perovskite annealing, probably owing to the increased grain size and decreased defects in absorber layer after thermal annealing. Due to the strong J - V hysteresis phenomena, we tracked the maximum power point of the both cells to evaluate the genuine power conversion efficiency. The steady-state output efficiency for cells without perovskite annealing initially stabilized at 2.2% and decreased slowly overtime due to the decreasing current density. The steady state output

for device with perovskite annealing stabilized at 8.6% after a slow increase in the first 20s.

So far there is still no consensus on the origin of the hysteresis in J - V curve, but several possibilities, such as interfacial trap states, mobile ions in perovskite, unbalanced charge flux etc., has been proposed to interpret the hysteresis.^[33-34] Increasingly efforts have been made to eliminate the hysteresis, and several approaches have been proven to be effective to get rid of the hysteresis. H. Snaith *et al* found that by inserting a thin layer of pyridine or self-assemble monolayer (SAM) between perovskite and TiO_2 , the steady-state output efficiency can be stabilized at backward measured efficiency.^[35-36] They clearly demonstrate the great potential of interfacial modification to get rid of the J - V hysteresis. Recently, we have also successfully eliminated the hysteresis in the cells prepared with the here presented thermal evaporation combined with spin coating method by additionally employing the concept of interfacial engineering, and the results will be discussed in detail elsewhere.

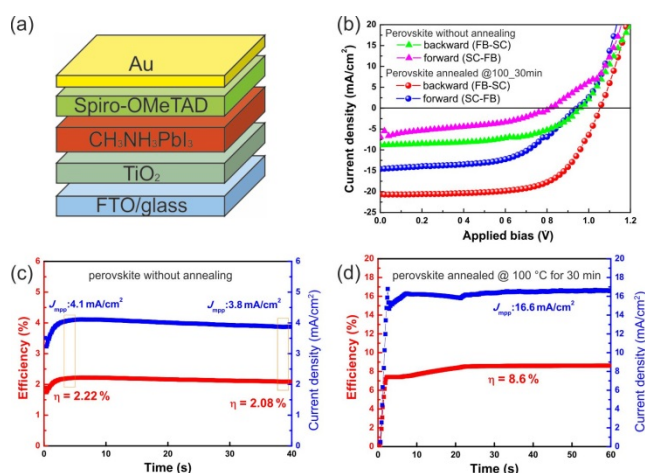


Figure 8 The device structure and photovoltaic performance. (a) Schematic illustration of cell structure. (b) Photovoltaic performance of devices without and with annealing step. Steady state output of device (c) without perovskite annealing and (d) with perovskite annealed at 100 °C for 30 min. All the devices are measured under simulated AM1.5G irradiation with 1000 W m^{-2} intensity. The J - V measurements are performed in both forward (1.2 V to -0.1 V) and backward (-0.1 V to 1.2 V) direction at a scan rate and delay time of 0.3 Vs^{-1} and 10 ms. The steady-state efficiency is evaluated by using a maximum power point tracker algorithm with constant AM1.5G illumination.

4 Conclusion We have developed a novel concept that employs porous nanostructured PbI_2 layers consisting of nanoplates for rapid growth of single phase planar $\text{CH}_3\text{NH}_3\text{PbI}_3$ layers. The controlled growth of PbI_2 nanoplates via thermal evaporation combined with spin coating of $\text{CH}_3\text{NH}_3\text{I}$ solution permits fast and complete formation of planar perovskite layer. We unravel that the intrinsic crystallographic structure of deposited material, crystal

characteristic of the underlying substrate, and deposition method are critical for achieving the porous nanostructured PbI_2 film comprising nanoplates. Planar perovskite solar cells prepared in the described method deliver power conversion efficiency of 8.6% at maximum power point. This work opens a new route for rapid preparation of other three dimensional organic-inorganic hybrid perovskites by rational designing the metal halide morphology.

Supporting Information Supporting Information is available from the Wiley Online Library or from the author. [Further details of the crystal structure investigations may be obtained from the Fachinformationszentrum Karlsruhe, 76344 Eggenstein-Leopoldshafen (Germany), on quoting the depository number ICSD-24262, ICSD-36170, ICSD-81976.] The crystallographic information file (.cif) for simulated $\text{CH}_3\text{NH}_3\text{PbI}_3$ XRD is obtained from supporting information in reference 37.

Acknowledgements We thank Dr. Fabian Pianezzi for incorporating the mpp tracking possibility into the J - V setup. Financial supports from Swiss National Science Foundation (SNF)-NRP70 (PV2050, 407040-154014) as well as from SNF-NanoTera and Swiss Federal Office of Energy (SYNERGY) are gratefully acknowledged. F. Fu would like to thank the Chinese Scholarship Council (CSC) for the financial support.

References

- [1] M. A. Green, A. Ho-Baillie, H. J. Snaith, *Nature Photon.* **8**, 506 (2014).
- [2] C. Wehrenfennig, G. E. Eperon, M. B. Johnston, H. J. Snaith, L. M. Herz, *Adv. Mater.* **26**, 1584 (2014).
- [3] S. D. Stranks, G. E. Eperon, G. Grancini, C. Mene-laou, M. J. P. Alcocer, T. Leijtens, L. M. Herz, A. Petrozza, H. J. Snaith, *Science* **342**, 341(2013).
- [4] A. Kojima, K. Teshima, Y. Shirai, T. Miyasaka, *J. Am. Chem. Soc.* **131**, 6050 (2009)
- [5] H. S. Kim, C. R. Lee, J. H. Im, K. B. Lee, T. Moehl, A. Marchioro, S. J. Moon, R. H. Baker, J. H. Yum, J. E. Moser, M. Graetzel, N. G. Park, *Sci. Rep.* **2**, 591. (2012).
- [6] M. Z. Liu, M. B. Johnston, H. J. Snaith, *Nature* **501**, 395 (2013).
- [7] J. Burschka, N. Pellet, S. J. Moon, R. H. Baker, P. Gao, M. K. Nazeeruddin, M. Graetzel, *Nature* **499**, 316 (2013).
- [8] N. J. Jeon, J. H. Noh, Y. C. Kim, W. S. Yang, S. Ryu, S. Seok, *Nat. Mater.* **13**, 897 (2014).

- [9] NREL, Best efficiency chart, http://www.nrel.gov/ncpv/images/efficiency_chart.jpg, accessed: December, 2014.
- [10] N. J. Jeon, J. H. Noh, W. S. Yang, Y. C. Kim, S. Ryu, J. Seo, S. Seok, *Nature* **517**, 476 (2015).
- [11] Z. G. Xiao, Q. F. Dong, C. Bi, Y. C. Shao, Y. B. Yuan, J. S. Huang, *Adv. Mater.* **26**, 6503(2014).
- [12] J. Seo, S. Park, Y. C. Kim, N. J. Jeon, J. H. Noh, S. C. Yoon and S. Seok, *Energy Environ. Sci.* **7**, 2642 (2014)
- [13] Z. P. Zhou, Q. Chen, G. Li, S. Luo, T. Song, H. S. Duan, Z. R. Hong, J. B. You, Y. S. Liu, Y. Yang, *Science* **345**, 542 (2014)
- [14] O. Malinkiewicz, C. R. Carmona, A. Soriano, E. Bandiello, L. Camacho, M. K. Nazeeruddin, H. J. Bolink, *Adv. Energy. Mater.* **4**, 1400345 (2014).
- [15] D. B. Mitzi, *Prog. Inorg. Chem.* **48**, 1-121. (1999).
- [16] Q. Wang, Y. C. Shao, Q. F. Dong, Z. G. Xiao, Y. B. Yuan, J. S. Huang, *Energy Environ. Sci.* **7**, 2359 (2014).
- [17] Q. Chen, H. P. Zhou, Z. R. Hong, S. Luo, H. S. Duan, H. H. Wang, Y. S. Liu, G. Li, Y. Yang, J. Am. Chem. Soc. **136**, 622 (2014).
- [18] X. G. Xiao, C. Bi, Y. C. Shao, Q. F. Dong, Q. Wang, Y. B. Yuan, C. G. Wang, Y. L. Gao, J. S. Huang, *Energy Environ. Sci.* **7**, 2619 (2014).
- [19] C. H. Chiang, Z. L. Tseng, C. G. Wu, *J. Mater. Chem. A* **2**, 15897 (2014).
- [20] J. H. Im, I. H. Jang, N. Pellet, M. Gratzel, N. G. Park, *Nat. Nanotechnology* **9**, 927 (2014).
- [21] K. N. Liang, D. B. Mitzi, M. T. Prikas, *Chem. Mater.* **10**, 403 (1998).
- [22] P. Docampo, F. C. Hanusch, S. D. Stranks, M. Dobliger, J. M. Feckl, M. Ehrensperger, N. K. Minar, M. B. Johnston, H. J. Snaith, T. Bein, *Adv. Energy Mater.* **4**, 1400355 (2014).
- [23] Y. Z. Wu, A. Islam, X. D. Yang, C. J. Qin, J. Liu, K. Zhang, W. Q. Peng, L. Y. Han, *Energy Environ. Sci.* **7**, 2934 (2014).
- [24] Y. H. Chen, T. Chen, L. M. Dai, *Adv. Mater.* **27**, 1053 (2015).
- [25] Y. N. Xia, Y. J. Xiong, B. Lim, S. E. Skrabalak, *Angew. Chem. Int. Ed.* **48**, 60 (2009).
- [26] T. Baikie, Y. N. Fang, J. M. Kadro, M. Schreyer, F. X. Wei, S. G. Mhaisalkar, M. Graetzel, T. J. White, *J. Mater. Chem. A* **1**, 5628 (2013).
- [27] S. Yang, Y. Zheng, Y. Hou, X. Chen, Y. Chen, Y. Wang, H. Zhao, H. Yang, *Chem. Mater.* **26**, 6705 (2014).
- [28] M. Schieber, N. Zamoshchik, O. Khakhan, A. Zuck, *J. Crys. Growth* **310**, 3168 (2008).
- [29] Y. Xia, Y. Xiong, B. Lim, S. E. Skrabalak, *Angew. Chem. Int. Ed.* **48**, 60 (2009).
- [30] R. Carel, Dissertation. Massachusetts Institute of Technology, September, **1995**
- [31] C. V. Thompson, *Annu. Rev. Mater. Sci.* **20**, 24 (1990).
- [32] C. V. Thompson, R. Carel, *Mater. Sci. & Engi B* **32**, 211 (1995).
- [33] H. J. Snaith, A. Abate, J. M. Ball, G. E. Eperon, T. Leijtens, N. K. Noel, S. D. Stranks, J. T. W. Wang, K. Wojciechowski, W. Zhang, *J. Phys. Chem. Lett.* **5**, 1511 (2014).
- [34] J. H. Heo, H. J. Han, D. Kim, T. K. Ahn, S. H. Im, *Energy Environ. Sci.* **8**, 1602 (2015),.
- [35] K. Wojciechowski, S. D. Stranks, A. Abate, G. Sadoughi, A. Sadhanala, Nikos Kopidakis, G. Rumbles, C. Z. Li, R. H. Friend, A. K. Y. Jen, H. J. Snaith, *ACS Nano* **8**, 12701 (2014).
- [36] N. K. Noel, A. Abate, S. D. Stranks, E. S. Parrott, V. M. Burlakov, A. Goriely, H. J. Snaith, *ACS Nano* **8**, 9815 (2014).
- [37] C. C. Stoumpos, C. D. Malliakas, M. G. Kanatzidis, *Inorg. Chem.* **52**, 9019 (2013).

Supporting Information

Controlled Growth of PbI_2 Nanoplates for Rapid Preparation of $\text{CH}_3\text{NH}_3\text{PbI}_3$ in Planar Perovskite Solar Cells

Fan Fu, Lukas Kranz, Songhak Yoon, Johannes Loeckinger, Timo Jäger, Julian Perrenoud, Thomas Feurer, Christina Gretener, Ayodhya N. Tiwari and Stephan Buecheler**

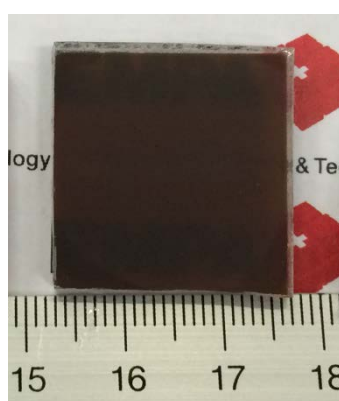
Figure S1. Photograph of evaporated PbI_2 film and as-deposited $\text{CH}_3\text{NH}_3\text{PbI}_3$ film on $\text{TiO}_2/\text{FTO}/\text{glass}$ substrate

Thermal evaporated PbI_2



(a)

As-deposited $\text{CH}_3\text{NH}_3\text{PbI}_3$



(b)

Figure S2. XRD patterns of as-deposited film with various $\text{CH}_3\text{NH}_3\text{I}$ concentrations. The PbI_2 thickness is around 200 nm as controlled by quartz crystal balance.

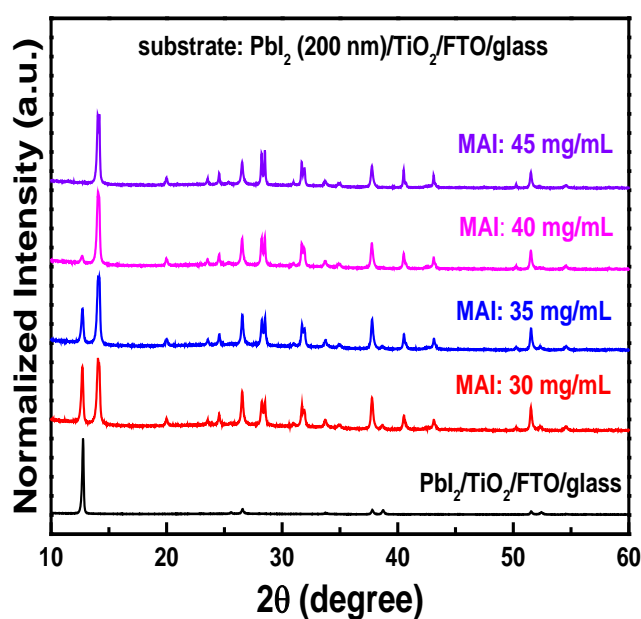


Figure S3. The XRD patterns and absorption spectra of samples with various annealing conditions.

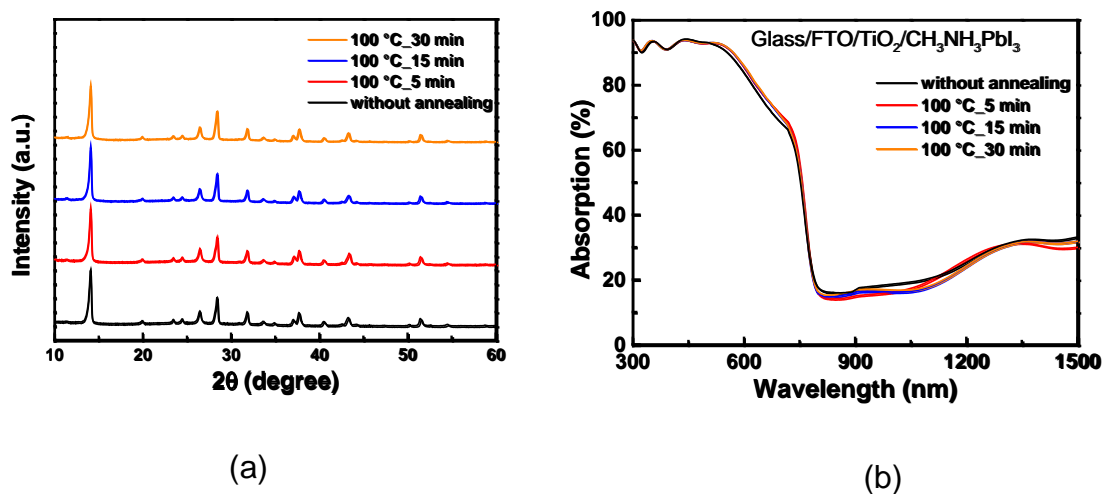


Figure S4. The XRD patterns of as-spin coated layer using various $\text{CH}_3\text{NH}_3\text{I}$ concentration on (a) PEDOT:PSS, (b) CuSCN, (c) glass, and (d) ZnO underlying substrate.

